Laminar-Forced Convection Mass Transfer to Ordered and Disordered Single Layer Arrays of Spheres

D. Ambesi and C.R. Kleijn
Dept. of Multi-Scale-Physics, J.M. Burgers Centre for Fluid Mechanics and Delft Process Technology Institute, Delft University of Technology, Leeghwaterstraat 39, Delft, 2628 CB, The Netherlands

DOI 10.1002/aic.13904
Published online September 7, 2012 in Wiley Online Library (wileyonlinelibrary.com).

Laminar forced convection mass transfer to single layers of equidistantly and nonequidistantly spaced spheres perpendicular to the flow direction is studied. Average Sherwood numbers are reported as a function of geometric configurations and flow conditions, for open frontal area fractions between 0.25 and 0.95, Schmidt numbers between 0.7 and 10, and Reynolds numbers (based on the sphere diameter and the free stream velocity) between 0.1 and 100. For equidistantly spaced arrays of spheres, a general analytical expression is proposed for the average Sherwood number as a function of the Reynolds number, Schmidt number and the open frontal area fraction, as well as asymptotic scaling rules for small and large Reynolds. For all studied Schmidt numbers, equidistant arrays exhibit decreasing average Sherwood numbers for decreasing open frontal area fractions at low Reynolds numbers. For high Reynolds numbers, the Sherwood number approaches that of a single sphere, independent of the open frontal area fraction. For equal open frontal area fractions, the Sherwood number in nonequidistant arrays is lower than in equidistant arrays for intermediate Reynolds numbers. For very low and high Reynolds numbers, nonuniformity does not influence mass transfer. © 2012 American Institute of Chemical Engineers *AIChE J*, 59: 1400–1408, 2013
Keywords: activated carbon, particles, filter, filtration, protective clothing

Introduction

Despite its practical relevance for applications such as low pressure drop activated carbon filters[1] and Chemical-Biological-Radiological-Nuclear protective clothing,[2] where single layers of loosely packed carbon particles are used to filter polluted air flows,[3,4] convective heat and mass transfer to spheres arranged in a single 2-dimensional (2-D) layer perpendicular to the flow direction has not yet been widely studied.

In contrast, a vast amount of studies on heat and mass transfer in 3-D packed beds of spheres[5–12] and on 1-D linear arrays of spheres aligned with the flow direction[13–21] can be found in literature.

Studies on 1-D linear arrays of spheres aligned with the flow direction,[13–21] cover a range of free-stream particle based Reynolds numbers from 1 to 1,700, and Schmidt (or Prandtl) numbers from 0.7 to 70. The number of particles in the linear array varied from 2 to 8, and the interparticle distance was varied from 1 to 10 particle diameters. In most studies all particles were of equal size. Wang and liu[19] and Tsai and Sterling[17] additionally studied the influence of differences in particle sizes. General conclusions from the mentioned studies are: (i) The average Nusselt/Sherwood number increases with increasing Reynolds number; (ii) The average Nusselt/Sherwood number increases with increasing interparticle distance; (iii) At Peclet numbers below 50, the average Nusselt/Sherwood is smaller than that for a single sphere; (iv) The Nusselt/Sherwood for the leading sphere may exceed that of a single sphere.

Of the vast amount of studies on heat and mass transfer in 3-D packed beds of spheres,[5–12] relatively few studies have been devoted to the effect of the precise particle packing structure.

In their classic experimental study, Thoenes and Kramers[8] studied mass transfer to a single active sphere placed in various regular packing arrangements of similar, but inactive spheres. For hydraulic diameter-based Reynolds number between 1 and 10^4 and different gases and liquids as working fluids, it was found that the Sherwood number increases with increasing distance between active and inert spheres.

For a fixed bed of particles in a cylindrical tube and particle Reynolds numbers between 100 and 700, Dixon and van Dongeren[9] showed that the ratio between the tube diameter and the particle diameter has a significant influence on heat transfer.

In a computational study of the fluid flow through packed beds of spheres in simple cubic, rhombohedral and face or body-centered structures at particle based Reynolds numbers between 12 and 2,000, Gunjal et al.[10] found that the local Nusselt number increases with increasing particle Reynolds numbers and increasing bed voidage.

Heat transfer in uniformly and nonuniformly packed beds of ellipsoidal and spherical particles was investigated by Yang et al.[11] for free stream particle based Reynolds numbers from 1 to 5,000 and a Prandtl number of 0.7. The

Correspondence concerning this article should be addressed to D. Ambesi at D.Ambesi@TUDelft.nl.

average Nusselt number was found to be dependent on the particle shape and packing structure. For a particular particle shape, the overall heat transfer was found to be maximum for a simple cubic packing. For a fixed packing structure, long elliptic particles gave the highest heat transfer. Uniform packings were found to have higher heat transfer than non-uniform packings with the same particle shape and packing density.

Whereas most work on packed bed has focussed on average Sherwood numbers, Guo et al.[12] in their numerical study focus on local variations in mass transfer rates. The authors concluded that there is a clear relationship between local pore structure, streamline patterns, and mass transfer rates.

In this article, we study mass transfer to 2-D single layer arrays of spheres perpendicular to the flow direction. We performed numerical simulations of the (steady-state or time-periodic) laminar incompressible flow and mass transfer around spheres arranged in an ordered or disordered single layer perpendicular to the flow direction, and we present sphere-averaged, steady-state or time-averaged, Sherwood numbers for mass transfer. The free stream Reynolds number, based on the sphere diameter and the free stream velocity, was varied between 0.1 and 100, and the Schmidt number between 0.7 and 10. Our work is of direct relevance for the design and optimization of low pressure drop carbon filters, and Chemical-Biological-Radiological-Nuclear protective clothing.

Numerical Approach

Studied configurations and boundary conditions

Figure 1 shows the computational domains for the three studied configurations, like (i) equidistantly spaced spheres arranged in a square pattern, (ii) equidistantly spaced spheres arranged in a hexagonal pattern, and (iii) nonequidistantly spaced spheres arranged in a disordered pattern. In all cases, the particles are arranged in a plane perpendicular to the flow direction.

The spheres are solid and nonpermeable and all have the same, constant diameter d. The total length of the computational domain along the streamwise direction x is $L_1 + 41d$, out of which L_1 upstream, and $40d$ downstream from the layer of spheres. The upstream length L_1 was chosen long enough to have a purely convective mass inflow through the inlet of the domain, that is, $L_1 > 10D/u_\infty$ where D is the mass diffusivity and u_∞ the free stream velocity. In the inlet, we imposed a constant tracer species mass fraction $C_\infty \ll 1$, and a uniform inlet velocity u_∞. The outlet plane was considered to be sufficiently far downstream from the layer of spheres, such that a constant pressure, zero axial concentration gradient and uniform streamwise velocity could be assumed constant across the outlet.

On the sphere walls, the tracer species is assumed to be consumed at infinite rate, so a zero concentration $C_w = 0$ and no-slip conditions for the velocity were imposed. The bounding sides of the computational domain, aligned with the streamwise direction x, were specified as symmetry boundaries in the case of equidistantly spaced spheres, or as periodic boundaries for layers of nonequidistantly spaced spheres.

The fluid properties (density ρ, viscosity μ, and mass diffusivity D) were assumed to be constant and buoyancy effects were neglected. The free stream Reynolds number was defined as $\mathrm{Re}_\infty = \rho u_\infty d/\mu$, the Schmidt number as $\mathrm{Sc} = \nu/D$. We also define a Reynolds number $\mathrm{Re}_L = \rho(u_\infty/\varepsilon)d/\mu = \mathrm{Re}_\infty/\varepsilon$ based on the average velocity u_∞/ε in the plane of smallest cross section.

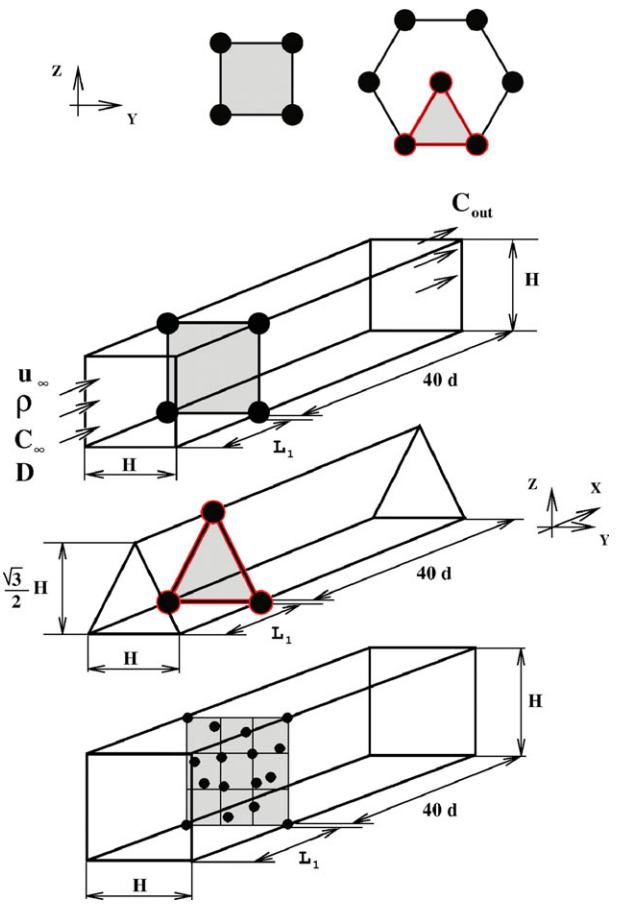

Figure 1. Computational domain.

[Color figure can be viewed in the online issue, which is available at wileyonlinelibrary.com.]

We study ordered layers of equisized spheres arranged in a square or hexagonal pattern, as well as disordered layers of $n_T = n_L^2$ equisized spheres, nonequidistantly distributed in a single square layer of width and height H as shown in Figure 1. For a prescribed open frontal area fraction ε, the domain size H follows from

$$\varepsilon = 1 - n_T \frac{\pi}{\beta}\left(\frac{d}{H}\right)^2 \tag{1}$$

where n_T equals 1 for ordered layers, and we used $n_T = n_L^2 = 16$ for the disordered layers. For the (ordered and disordered) square layers, $\beta = 4$, for the triangular layer, $\beta = 4\sqrt{3}$. To generate patterns with a controlled level of disorder, the following procedure was applied, see Figure 2: first, the spheres are placed on a square grid of $n_y = n_L$ columns by $n_z = n_L$ rows. In this configuration the intersphere distances are constant and equal to $\delta_y = \delta_z = \bar{\delta} = H/n_L - d$.

Then, for each column, we redistribute the spheres such that the standard variation in the intersphere distances equals $\sigma = \alpha\bar{\delta}$, where α is our disorder control variable, which equals zero for ordered arrays of spheres, whereas larger values of α lead to increased disorder. For given values of n_L,

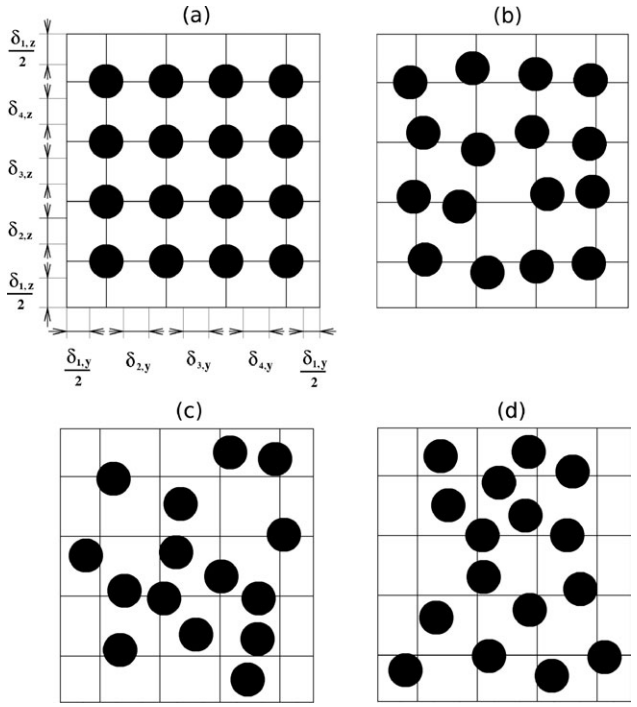

Figure 2. Ordered and disorder arrays of n_T = 16 spheres for ε = 0.8: (*a*) ordered (α = 0); (*b*) one realization for α = 0.5; (*c*) one realization for α = 1; (*d*) a second realization for α = 1.

$\bar{\delta}$, and α, an infinite number of distributions can be generated that obey the following equations for $\bar{\delta}$ and σ:

$$\sum_{i=1}^{n_L} \delta_{i,z} = n_L \bar{\delta} \tag{2}$$

$$\sum_{i=1}^{n_L} \delta_{i,z}^2 = n_L(\sigma^2 + \bar{\delta}^2) \tag{3}$$

To obtain distributions of n_L spheres with specified $\bar{\delta}$ and $\sigma = \alpha\bar{\delta}$, we draw the values of $\delta_{1,z}$, $\delta_{2,z}\ldots\delta_{n_L\text{-}2,z}$ from a normal probability distribution with the desired values of σ and $\bar{\delta}$. Subsequently, the values of $\delta_{n_L\text{-}1,z}$ and $\delta_{n_L,z}$ are obtained by solving Eqs. 2 and 3. Repeating this procedure for different random values of $\delta_{1,z}$, $\delta_{2,z}\ldots\delta_{n_L\text{-}2,z}$ results in different realizations of the configuration with the same $\bar{\delta}$ and α.

After the spheres in each column have been randomly redistributed according to the above procedure, the same procedure is applied to redistribute the spheres in each row. We only accept those distributions in which no spheres overlap or touch, and all spheres lay within the $H \times H$ square. The first is physically impossible in a single layer distribution, the second is highly improbable and would create difficulties in creating a numerical mesh. The third restriction imposed on the distributions leads to some disturbance of the pure randomness of the distributions, as it may create larger voids near the edges, especially for large α. However, the purpose of our study of nonuniform distributions is precisely to show the impact of such large voids. Figure 2 shows an ordered layer for $\varepsilon = 0.8$ and $n_L = 4$, as well as examples of disordered layers with $\varepsilon = 0.8$, and $\alpha = 0.5$ and 1.0, respectively.

Meshing of the 3-D computational domain was performed in Gambit.[22] The meshes consisted of 220,000 to 1,800,000 hexahedral and tetrahedral grid cells, and local grid refinement was applied in the regions nearby the surfaces of the spheres and in the interstitial spaces between the spheres.

The solver

The flow was assumed laminar and incompressible, thus the continuity equation is expressed as

$$\nabla \cdot \vec{u} = 0 \tag{4}$$

where $\vec{u}$ is the velocity field vector.

Assuming gravity effects negligible and no external body forces, the Navier–Stokes (momentum) equations can be written as

$$\rho \frac{\partial \vec{u}}{\partial t} + \rho(\nabla \cdot \vec{u}\vec{u}) = -\nabla P + \nabla \cdot \bar{\bar{\tau}} \tag{5}$$

where $\bigtriangledown P$ and $\bar{\bar{\tau}}$ are, respectively, the pressure field gradient and the viscous stress tensor for a Newtonian fluid.

The species transport equation, assuming constant species diffusivity, reads

$$\frac{\partial C}{\partial t} + \vec{u} \cdot \nabla C = D\nabla^2 C \tag{6}$$

where C is the species concentration.

Equations 4–6 were solved in 3-D, steady-state or transient formulation. The latter was needed for cases with large Reynolds numbers and small intersphere distances, in which the interaction between the sphere wakes leads to vortex instability behind the spheres as reported by Kim et al.[23] and Hill et al.[24] For large intersphere distances, however, the sphere wakes are noninteracting and stable for all Reynolds numbers studied.

A second order QUICK scheme[25] was used to discretize the equations in space, whilst a second order implicit time discretization scheme was used.[26] The pressure field was obtained by using the SIMPLE algorithm.[27] Convergence limits for the sum of the normalized absolute residuals (i.e., the absolute values of the residuals per grid point, summed over all grid points, and normalized by the value of that same summation at the beginning of the iterative solution procedure) for all the equations were set to 10^{-6}. For the unsteady simulations, 10^{-6} normalized residuals convergence was assured at each time step. Unsteady simulations were continued until a time-periodic, pseudo steady-state in the downstream velocity and concentration profiles was reached.

For a number of representative cases ($\mathrm{Re}_\infty = 0.1$, $\varepsilon = 0.8$; $\mathrm{Re}_\infty = 10$, $\varepsilon = 0.4$; $\mathrm{Re}_\infty = 100$, $\varepsilon = 0.25$) with uniform sphere distributions, we studied the dependence of our results on grid refinement, time step size and discretization scheme. Doubling the number of grid cells in all coordinate directions (from 400,000 to 3,200,000, 230,000 to 1,800,000, and 300,000 to 2,312,000, respectively), halving the time step size (from $\Delta t = 0.3d/u_\infty$ to $\Delta t = 0.15d/u_\infty$), doubling the length of the upstream and downstream domain (from L_1 to $2L_1$ and from $40d$ to $80d$, respectively), and switching from QUICK to second order upwind schemes led to differences in the computed Sherwood number of less than 10% as shown in Table 1 for some of the above configurations.

Table 1. Dependence of Sh on Grid Refinements and Domain Length for Uniformly Spaced Spheres, Sc = 0.7

ε	Re_∞	Δt	Nr. of Grid Cells	Upstream Domain Length	Downstream Domain Length	Sh
0.25	100	$0.3d/u_\infty$	300,000	$10u_\infty/D$	$40d$	9.3411
0.25	100	$0.15d/u_\infty$	300,000	$10u_\infty/D$	$40d$	9.3425
0.25	100	$0.3d/u_\infty$	2,312,000	$10u_\infty/D$	$40d$	9.3969
0.4	10	$0.3d/u_\infty$	230,000	$10u_\infty/D$	$40d$	2.4378
0.4	10	$0.3d/u_\infty$	1,800,000	$10u_\infty/D$	$40d$	2.6914
0.8	0.1	$0.3d/u_\infty$	400,000	$10u_\infty/D$	$40d$	0.0752
0.8	0.1	$0.3d/u_\infty$	890,000	$20u_\infty/D$	$80d$	0.0775

Sherwood number

A steady-state mass balance over the domain sketched in Figure 1, assuming constant fluid properties and a purely convective inflow and outflow, leads to

$$n_T \pi d^2 k (C_\infty - C_w) = u_\infty \frac{\beta}{4} H^2 (C_\infty - C_{out}) \tag{7}$$

where C_∞, C_{out}, and C_w are the tracer species inlet concentration, mass averaged outflow concentration, respectively, and sphere wall concentration, and k the average mass transfer coefficient. With Eq. 1, this leads to the following relation for the average Sherwood number

$$Sh = \frac{kd}{D} = \frac{u_\infty d(C_\infty - C_{out})}{4D(1-\varepsilon)(C_\infty - C_w)} \tag{8}$$

where D is the tracer species diffusivity. For $\varepsilon \to 1$, C_{out} will approach C_∞ and the Sh values are expected to approach that of a single sphere.

Results and Discussion

In the following two subsections, we present results for, respectively, equidistantly and nonequidistantly spaced spheres arranged in a single layer perpendicular to the flow direction. Sherwood numbers will be correlated with the free-stream and local Reynolds numbers Re_∞ and $Re_L = Re_\infty/\varepsilon$ and the Schmidt number, for various values of the open frontal area fraction ε and the nonuniformity parameter α. The Schmidt number is varied from 0.7 to 10, and the free stream Reynolds number Re_∞ from 0.1 to 100. For hexagonally and squarely arranged equidistant arrays, we varied the open frontal area fraction from $\varepsilon = 0.25$ to 0.95. For the nonequidistant arrays we studied open frontal area fractions $\varepsilon = 0.4$ and 0.8 and nonuniformity parameters $\alpha = 0.5$, 1.0, and 1.5.

Equidistant arrays

For all studied values of Re_∞, Sc, and ε, only small differences were found between the average Sherwood numbers in the ordered square and hexagonal arrays. Differences in Sherwood numbers between these two arrangements were less than 15% for all studied cases, as shown in Figure 3. Therefore, in the following, we will discuss in detail only the results obtained for square arrangements, and we will further focus our discussion on the much larger differences between the ordered arrangements on the one hand, and the disordered arrangements on the other hand.

Figure 4 shows the obtained Sherwood numbers as a function of Re_∞ and the open frontal area fraction ε for equidistantly spaced spheres arranged in square structures at Sc = 0.7. For a given open frontal area fraction ε, Sh increases with increasing Re_∞. For low values of Re_∞, Sh is much lower than for a single sphere (here evaluated by use of the empirical equation proposed by Whitaker[28])

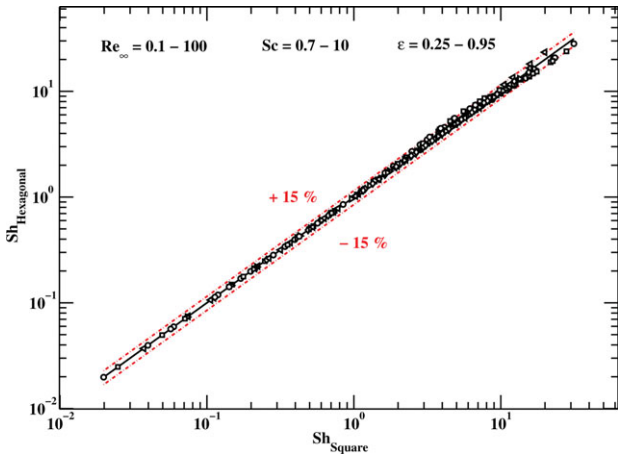

Figure 3. Sherwood number parity plot for equidistantly spaced spheres arranged in square and hexagonal structures.

[Color figure can be viewed in the online issue, which is available at wileyonlinelibrary.com.]

$$Sh_{Whitaker} = 2 + (0.4Re_\infty^{1/2} + 0.06Re_\infty^{2/3})Sc^{0.4} \tag{9}$$

and increases with increasing open frontal area fraction ε, that is with increasing interparticle distance. These observations are in agreement with the observations reported in literature for both 1-D arrays of spheres aligned with the flow, and 3-D arrays of packed spheres, as discussed in Section "Introduction". For large Re_∞, Sh approaches the values found for single spheres when ε is large, whereas for smaller ε it actually is somewhat larger than the values reported for single spheres. This was also reported for the leading spheres in linear arrays aligned with the flow.[16]

As the mass transfer to individual spheres is determined by local flow conditions near the spheres, rather than the

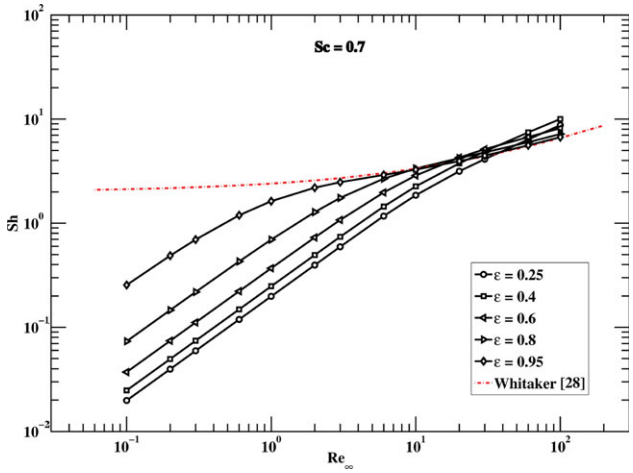

Figure 4. Sh number as a function of ε and Re_∞ for ordered arrays of spheres and Sc = 0.7.

Also shown is the correlation by Whitaker[28] for a single sphere. [Color figure can be viewed in the online issue, which is available at wileyonlinelibrary.com.]

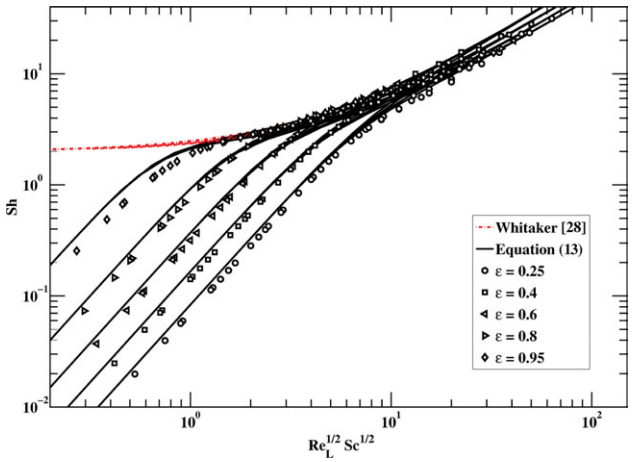

Figure 5. Sh number as a function of ε and $Re_L^{1/2}Sc^{1/2}$ for ordered arrays of spheres.

Also shown is the correlation by Whitaker[28] for a single sphere. [Color figure can be viewed in the online issue, which is available at wileyonlinelibrary.com.]

upstream free flow conditions, it is more informative to present Sh as a function of the local Reynolds number $Re_L = Re_\infty/\varepsilon$.

Figure 5 shows the obtained Sherwood numbers for equidistantly spaced spheres as a function of $Re_L^{1/2}Sc^{1/2}$, for different values of the open frontal area fraction ε. From this figure, four main observations can be made:

(i) For low $Re_L^{1/2}Sc^{1/2}$, Sherwood increases with increasing open frontal area fraction ε.

(ii) For high $Re_L^{1/2}Sc^{1/2}$, the Sherwood number is close to that of a single sphere (here evaluated by use of the empirical equation proposed by Whitaker[28] replacing Re_∞ by Re_L), and only slightly dependent of the open frontal area fraction ε.

(iii) The value of $Re_L^{1/2}Sc^{1/2}$ above which the Sherwood number is virtually independent of ε and close to that of a single sphere, decreases with increasing ε.

(iv) For large $Re_L^{1/2}Sc^{1/2}$, Sh values can be up to a factor two higher than those reported for a single sphere.

The latter observation can be understood from the fact that the interacting wakes at large Re_L lead to vortex instabilities which enhance mass transfer.

The first three observations can be understood and more quantitatively analysed by looking at the concentration distributions and concentration boundary layer formation around the spheres, as shown in Figure 6. This figure shows contours of the dimensionless concentration $\theta = (C - C_w)/(C_\infty - C_w)$, which varies from $\theta = 1$ in the inlet to $\theta = 0$ at the sphere walls.

For small Re and ε, for example, $Re_\infty = 10$ and $\varepsilon = 0.25$ in Figure 6, all incoming mass $u_\infty\beta/4H^2C_\infty$ is transferred by diffusion to the sphere surfaces, and the flow has essentially lost all the tracer concentration once it has crossed the sphere plane, even for open frontal areas as large as $\varepsilon = 0.95$. With $u_\infty\beta/4H^2C_\infty = ShD/dn_T\pi d^2C_\infty$ and $(H/d)^2 = (n_T\pi)/(\beta/(1-\varepsilon))$ this leads to

$$Sh = \frac{1}{4}\frac{Re_\infty Sc}{1-\varepsilon} = \frac{1}{4}Re_L Sc\frac{\varepsilon}{1-\varepsilon} \tag{10}$$

The low Re_L behavior as described above will occur when the convective time scale $d/(u_\infty/\varepsilon)$ in which the fluid passes the sphere plane is large compared to the transversal diffusion time scale $\left(\frac{1}{2}L\right)^2/D$, with $L \approx \sqrt{\varepsilon}H/n_L$ the average distances between the sphere surfaces, this leads to:

$$Re_L \ll Re_1 = \frac{4\beta}{\pi}\frac{1-\varepsilon}{\varepsilon}Sc^{-1} \tag{11}$$

The validity of Eqs. 10 and 11 is shown in Figure 7, in which all simulation results have been presented together.

For large Re and large ε, for example, $Re_\infty = 100$ and $\varepsilon = 0.8$ in Figure 6, the thickness $\delta_C \approx (1/0.4)Re_L^{-1/2}Sc^{-0.8}d$ of the concentration boundary layers that are formed around

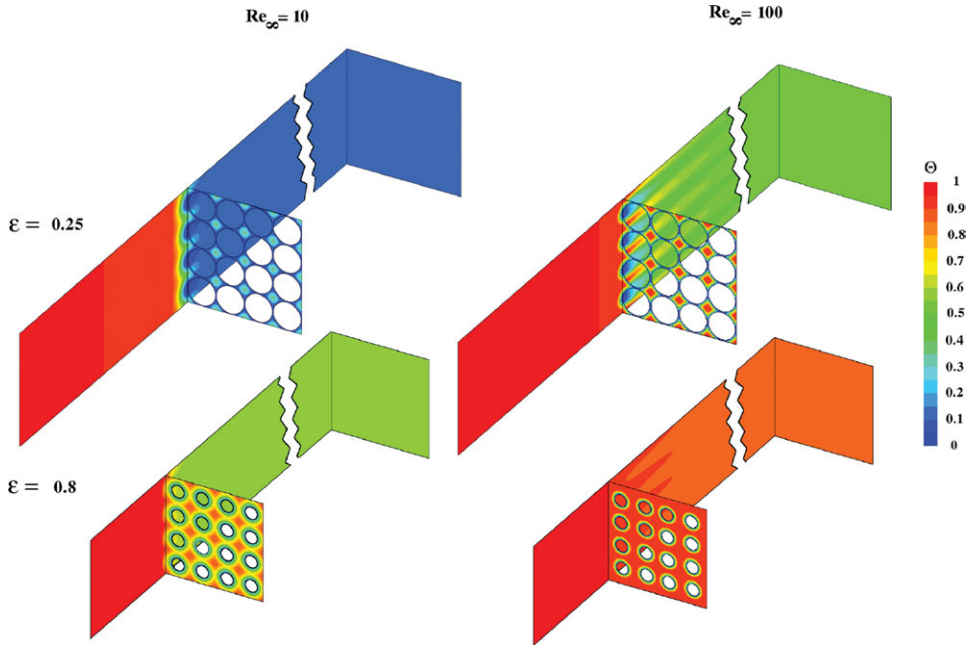

Figure 6. Dimensionless mass concentration contours for ordered spheres at Sc = 0.7.

[Color figure can be viewed in the online issue, which is available at wileyonlinelibrary.com.]

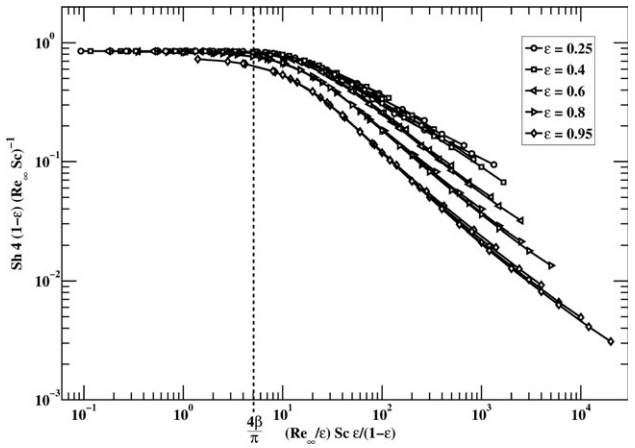

Figure 7. Illustration of Eqs. 10 and 11 for $0.1 \leq Re_\infty \leq 100$, $0.7 \leq Sc \leq 10$, and $0.25 \leq \varepsilon \leq 0.95$ for ordered spheres.

the spheres is thin compared to the inter-sphere distance L. As a result, the mass transfer to one sphere is not significantly influenced by the presence of the other spheres and therefore approaches that of a single sphere. Requiring that $\delta_C < 0.1L$, we find that this is the case for

$$Re_L \gg Re_2 \approx \frac{625\beta}{\pi}\frac{1-\varepsilon}{\varepsilon}Sc^{-0.8} \tag{12}$$

Figure 8, in which all simulations results have been combined, demonstrates that indeed the Sherwood numbers approach that of Whitaker's correlation for a single sphere when $Re_L\varepsilon/(1-\varepsilon)Sc^{0.8} > 625\beta/\pi$

In agreement with observation (iii), Eq. 12 shows that the critical value Re_2 above which the Sherwood number approaches that of a single sphere decreases with increasing Sc and with increasing ε.

All results presented in Figure 5 can be summarized by means of the correlation stated in Eq. 13, where Sh is described as a function of Re_L, Sc, and ε:

$$Sh = \frac{\frac{1}{4}\frac{\varepsilon}{1-\varepsilon}Re_L Sc}{\sqrt{1+\left(\frac{\frac{1}{4}\frac{\varepsilon}{1-\varepsilon}Re_L Sc}{Sh_{Whitaker}}\right)^2}} \tag{13}$$

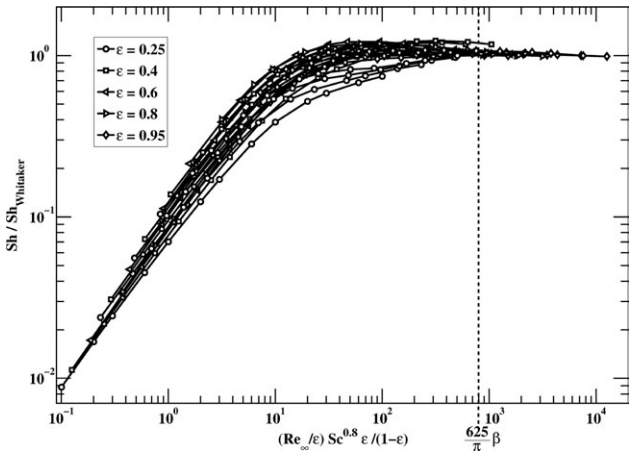

Figure 8. Ratio between Sh of ordered spheres and Sh of a single spheres[28] for $0.1 \leq Re_\infty \leq 100$, $0.7 \leq Sc \leq 10$, and $0.25 \leq \varepsilon \leq 0.95$

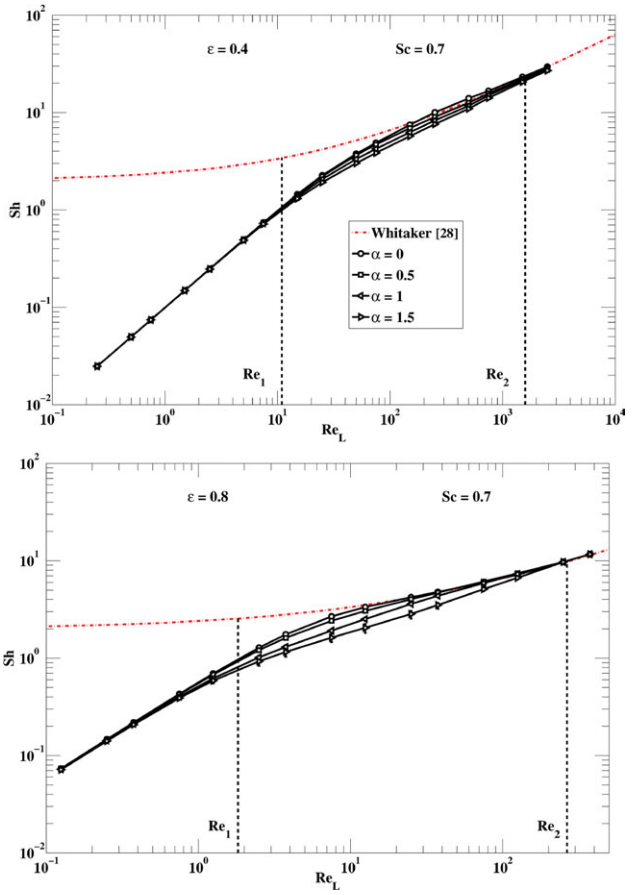

Figure 9. Sh as a function of ε, α and Re_L for disordered arrays of spheres at Sc = 0.7.

Values of Re_1 and Re_2 according to Eqs. 11 and 12 have been indicated by vertical dashed lines.

[Color figure can be viewed in the online issue, which is available at wileyonlinelibrary.com.]

where $Sh_{Whitaker}$ is the Sherwood correlation for a single sphere by Whitaker[28] given by Eq. 9 in which Re_∞ is replaced by $Re_L = Re_\infty/\varepsilon$. Sherwood numbers predicted by Eq. 13 have been included as solid lines in Figure 5, showing the good agreement with the simulation data.

Disordered arrays

Figures 9 and 10 show Sherwood numbers in disordered ($\alpha > 0$) arrays of spheres, compared to those in equidistantly spaced ($\alpha = 0$) arrays of spheres. The open frontal area fraction is $\varepsilon = 0.4$ and 0.8, the nonuniformity parameter $\alpha = 0$, 0.5, 1, and 1.5 and the Schmidt number is 0.7 and 10. For each combination of $\alpha > 0$ and ε, several different geometrical configurations were realized. The spread in Sherwood numbers between these different realizations is indicated by the vertical error bars.

Several general observation can be made:

(i) For high ($\gg Re_2$) and low ($\ll Re_1$)values of Re_L, the Sherwood number for nonequidistant spheres is equal to that for equidistant spheres.

(ii) For nonequidistantly spaced spheres, the Sherwood number is lower than for equidistantly spaced spheres at intermediate ($Re_1 < Re_L < Re_2$) values of Re_L. The Sherwood number can be up to a factor two lower compared to equidistant spheres.

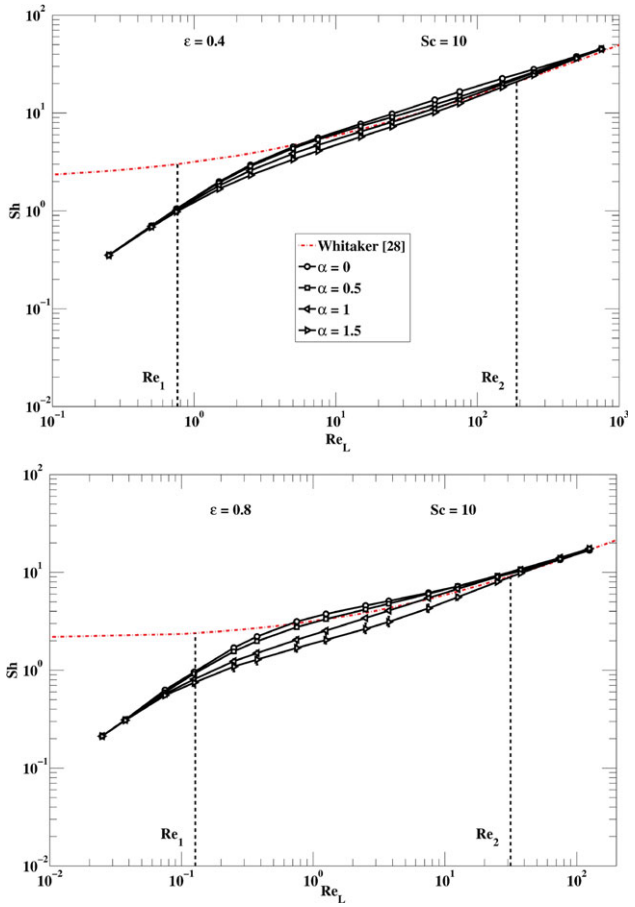

Figure 10. Sh as a function of ε, α and Re_L for disordered arrays of spheres at Sc = 100.

Values of Re_1 and Re_2 according to Eqs. 11 and 12 have been indicated by vertical dashed lines. [Color figure can be viewed in the online issue, which is available at wileyonlinelibrary.com.]

(iii) For low values of ε and α, the spread in Sherwood numbers between different geometry realizations is small. For high values of ε and α, the spread in Sherwood numbers is larger. However, the spread in Sherwood numbers for different geometric realizations at fixed α is small compared to the difference in Sherwood numbers at different values of α.

The above three observations can again be understood and more quantitatively analysed from the earlier analyses for equidistant spheres, and by looking at the concentration distributions and concentration boundary layer formation around non-equidistant spheres, as shown by contours of $\theta = (C - C_w)/(C_\infty - C_w)$ in Figure 11.

As was the case for equidistant spheres, at low values of Re_L, as in the left-hand column of Figure 11, virtually all incoming mass is transferred by diffusion to the spheres, with little dependence of the precise distribution of the spheres. As a result, *Sh* has little dependence on α for low values of Re_L. On the other hand, for large values of Re_L as in the right-hand column of Figure 11, thin, non-interacting boundary layers are formed around the individual spheres, and mass transfer is again independent of the precise distribution of the spheres. These arguments explain the above observation (*i*).

For intermediate values of Re_L, as in the central column of Figure 11, highly interacting concentration boundary layers are formed around the spheres, and mass transfer is locally reduced in regions of more dense packing of the spheres, and locally enhanced in regions of less dense packing. The relation between local Sherwood numbers and local packing densities can be analyzed through the relation between Sh and ε for equidistant spheres at intermediate values of Re_L, as presented in the previous section. This showed a strong, non linear, decrease of Sh with increasing packing density. The result of this nonlinear relationship between local Sh and local ε is that the average Sh in a non-equidistant array with given ε is lower than the average Sh

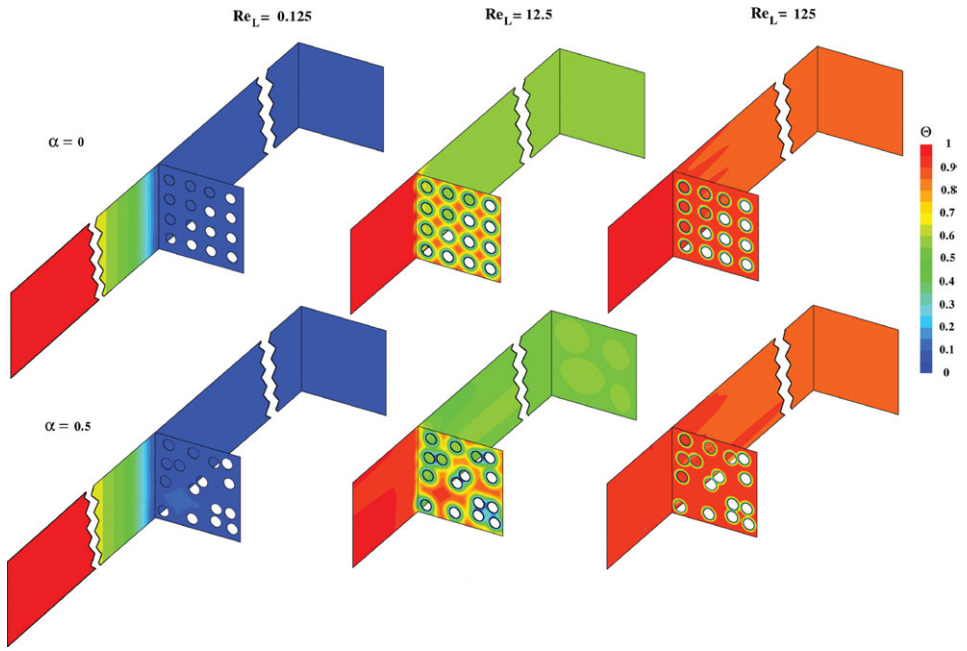

Figure 11. Dimensionless mass concentration contours for disordered spheres at ε = 0.8 and *Sc* = 0.7.

[Color figure can be viewed in the online issue, which is available at wileyonlinelibrary.com.]

in an equidistant array of equal ε for an intermediate range of Re_L, for which interacting concentration boundary layers are formed around the spheres. Similar to the analysis for equidistant spheres, and in agreement with the above observation (ii), Sh is found to be independent of α for $Re_L < Re_1$ and for $Re_L > Re_2$ (indicated by the vertical dashed lines in Figures 9 and 10).

Finally, for small values of α and ε, different geometry realizations at given ε and α will exhibit small geometric variations, explaining that there is little variation in Sherwood numbers. For large ε and α, however, there may be large geometric differences between different geometry realizations (compare, *e.g.*, Figs. 2c, d), explaining the observed larger variations in Sh numbers between geometrical configurations with the same value of α and ε.

Conclusions

For values of the local Reynolds number $Re_L = Re_\infty/\varepsilon$ (i.e., the free stream Reynolds number divided by the open frontal area fraction ε) that are larger than $Re_2 \approx 625\beta/\pi(1-\varepsilon)/\varepsilon Sc^{-0.8}$, laminar forced convection mass transfer to equidistantly and nonequidistantly spaced spheres in a single layer perpendicular to the flow direction is independent of the sphere packing density and sphere packing configuration, and can be accurately described by established Sherwood correlations for a single sphere when the Reynolds number in these correlations is replaced by Re_L.

For values of Re_L that are small compared to $Re_1 = 4\beta/\pi(1-\varepsilon)/\varepsilon Sc^{-1}$, Sh decreases strongly with increased packing density, and is given by $Sh = \varepsilon Re_L Sc/(4(1-\varepsilon))$, again independent of sphere packing configuration.

For the intermediate Re_L regime, that is $Re_1 < Re_L < Re_2$, Sh numbers in nonequidistantly spaced arrays of spheres can be up to a factor 2 lower as compared to equidistantly spaced arrays with the same open frontal area fraction.

Acknowledgments

The work in this article was supported by The Netherlands Organization for Applied Scientific Research TNO.

Notation

C_∞ = free stream mass fraction
C_w = sphere wall mass fraction
C_{out} = outlet section mass fraction
d = sphere diameter, *m*
D = mass diffusivity, m^2/s
H = domain height, *m*
k = mass transfer coefficient, *m/s*
n_L = number of spheres per row/column
n_T = total number of spheres
n_y = number of spheres per column
n_z = number of spheres per row
L = average distance between sphere surfaces, *m*
L_1 = distance between domain inlet and sphere surfaces, *m*
$\vec{u}$ = velocity vector, *m/s*
u_∞ = free stream fluid velocity, *m/s*
x = streamwise direction
α = dimensionless level of disorder
β = dimensionless constant
δ_y = sphere to sphere wall distance along *y* direction, *m*
δ_z = sphere to sphere wall distance along *z* direction, *m*
δ_C = concentration boundary layer thickness, *m*
$\bar{\delta}$ = sphere to sphere wall mean distance, *m*
ε = open frontal area fraction
θ = fluid mass fraction
μ = dynamic viscosity, $kg/(m/s)$
ν = kinematic viscosity, m^2/s
ρ = fluid density, kg/m^3
σ = standard deviation
$\bar{\bar{\tau}}$ = viscous stress tensor, *Pa*
Sh = Sherwood Number, *kd/D*
Sc = Schmidt Number, *v/D*
Re_∞ = Reynolds number, $u_\infty d/v$
Re_L = local Reynolds number, Re_∞/ε
Re_1 = low critical Reynolds number
Re_2 = high critical Reynolds number

Literature Cited

1. Davies CN. *Air Filtration*. London: Academic Press, 1973.
2. Brasser P. Modelling the chemical protective performance of NBC clothing material. *J Occup Environ Hyg*. 2004;1:620–628.
3. Brasser P, Kaaijk J. *The effect of air permeability on the chemical protective performance of NBC suits*. In: *Symposium of the NATO RTO Human Factors and Medecine Panel (HFM)*. Brussels: NATO Research and Technology Organization, 2002.
4. Brasser P, van Houwelingen T. Theoretical and experimental study of vapor deposition onto a dressed body part. *AIChE J*. 2008; 54:844–849.
5. Carberry J. A boundary-layer model of fluid-particle mass transfer in fixed beds. *AIChE J*. 1960;6:460–463.
6. Karabelas A, Wegner T, Hanratty T. Use of asymptotic relations to correlate mass transfer data in packed beds. *Chem Eng Sci*. 1971;26:1581–1589.
7. Pfeffer R, Happel J. An analytical study of heat and mass transfer in multiparticle systems at low Reynolds numbers. *AIChE J*. 1964;10:605–611.
8. Thoenes J, Kramers H. Mass transfer from spheres in various regular packings to a flowing fluid. *Chem Eng Sci*. 1958;8:271–283.
9. Dixon A, van Dongeren J. The influence of the tube and particle diameters at constant ratio on heat transfer in packed beds. *Chem Eng Process Process Intensification*. 1998;37:23–32.
10. Gunjal P, Ranade V, Chaudhari R. Computational study of a single-phase flow in packed beds of spheres. *AIChE J*. 2005; 51:365–378.
11. Yang J, Wang Q, Zeng M, Nkayama A. Computational study of forced convective heat transfer in structured packed beds with spherical or ellipsoidal particles. *Chem Eng Sci*. 2010;65:726–738.
12. Guo G, Liu G, Thompson K. Numerical analysis of the effects of local hydrodynamics on mass tansfer in heterogenous porous media. *Chem Eng Commun*. 2003;190:12:1641–1660.
13. Aminzadeh K, Al Taha T, Cornish A. Mass transport around two spheres at low Reynolds numbers. *Int J Heat Mass Trans*. 1974;17:1425–1436.
14. Reuven T, Dah N, Sirignano W. Heat and momentum transfer around a pair of spheres in viscous flow. *Int J Heat Mass Trans*. 1984;27:1953–1962.
15. Dalman M, Merkin J, McGreavy C. Fluid flow and heat transfer past two spheres in a cylindrical tube. *Comput Fluids*. 1986;14:267–281.
16. Ramachandran R, Kleinstreuer C, Wang T. Forced convection heat transfer of interacting spheres. *Numer Heat Trans Part A Appl*. 1989;15:4:471–487.
17. Tsai J, Sterling A. The application of and embedded grid to the solution of heat and momentum transfer for spheres in a linear array. *Int J Heat Mass Trans*. 1990;33:2491–2502.
18. Chiang H, Kleinstreuer C. Convection heat transfer of collinear interacting droplets with surface mass transfer. *Int J Heat Fluid Flow*. 1991;12.
19. Wang B, Liu T. Research on hydrodynamics and heat transfer for fluid around spheres in tandem. *Int J Heat Mass Trans*. 1992;35:307–317.
20. Lloyd B, Boehm R. Flow and heat transfer around a linear array of spheres. *Numer Heat Trans Part A Appl*. 1994;26:2: 237–252.
21. Maheshwari A, Chhabra R, Biswas G. Effect of blockage on drag and heat transfer from single sphere and an in-line array of three spheres. *Powder Technol*. 2006;168:74–83.
22. Gambit 2.2 Tutorial Guide 2004, Fluent Incorporated, Centerra Resource Park, 10 Cavendish Court, Lebanon, NH, 03766.

23. Kim I, Elghobashi S, Sirignano W. Three-dimensional flow over two spheres placed side by side. *J Fluid Mech*. 1993;246:465–488.
24. Hill R, Koch D, Ladd A. Moderate Reynolds number flows in ordered and random arrays of spheres. *J Fluid Mech*. 2001;448:243–278.
25. Leonard BP, Mokhtari S. ULTRA-SHARP Nonoscillatory Convection Schemes for High-Speed Steady Multidimensional Flow. *Tech. rep*., NASA Lewis Research Center, 1990. NASA TM 1–2568 (ICOMP-90-12).
26. Barth T, Jespersen D. The design and application of upwind schemes on unstructred meshes. In: *AIAAA 27th Aerospace Sciences Meeting*. Reno, Nevada, USA. 1989.
27. Fluent 6.3 Tutorial Guide 2006, Fluent Incorporated, Centerra Resource Park, 10 Cavendish Court, Lebanon, NH, 03766.
28. Whitaker S. Forced convection heat transfer correlations for flow in pipes, past flat plates, single cylinders, single spheres, and for flow in packed beds and tube bundles. *AIChE J*. 1972;18:361–371.

Manuscript received Feb. 14, 2012, and revision received July 26, 2012.